EDGE ARTICLE

Check for updates

All publication charges for this article have been paid for by the Royal Society of Chemistry

Atomic Ce sites promote a four-electron pathway of Pt as NADH oxidase mimics for *in situ* coenzyme regeneration

Yinjun Tang,[a] Yifei Chen,[a] Pengcheng Qi,[b] Ruimin Li,[a] Wenxuan Jiang,[a] Hongcheng Sun, [iD][c] Wenling Gu[a] and Chengzhou Zhu [iD] *[a]

Nicotinamide adenine dinucleotide (NAD^+) is a key coenzyme for human redox reactions, vital for cellular health and metabolic balance. Lots of NAD^+-dependent redox enzymes, like alcohol dehydrogenase (ADH) and lactate dehydrogenase, can catalyze both forward and reverse reactions. However, substrate accumulation and inadequate NAD^+ replenishment hinder forward reactions, disrupting the proper metabolism of these substrates. In this work, we reported atomic Ce-doped Pt (Ce_1Pt) nanoparticles with abundant oxygen vacancy sites to boost NADH oxidase (NOX)-like activity for coenzyme regeneration. Mechanistic studies reveal that atomic Ce doping increases electron density of Pt and surface defects, enhancing O_2 adsorption and accelerating the rate-limiting step. Furthermore, Ce_1Pt employs a $4e^-$ pathway for O_2 reduction during NADH oxidation, minimizing toxic H_2O_2 byproducts and improving detection accuracy by reducing oxidative interference. Finally, Ce_1Pt enables NAD^+ regeneration and substrate metabolism, offering a promising strategy to counteract excessive alcohol intake or lactate accumulation. Through competitive adsorption between the reduced coenzyme NADH of ADH and chromogenic substrates, a microfluidic device integrated with immobilized Ce_1Pt achieves blood alcohol detection with a low limit of detection of 0.012 mM.

Introduction

Nicotinamide adenine dinucleotide (NAD^+) plays a crucial role in the human body by participating in various biochemical reactions, particularly in cellular metabolism and energy production.[1] The human body regulates energy metabolism, redox reactions, and overall cellular health by maintaining the balance between NAD^+ and NADH.[2,3] However, impairment of the body's health, for instance, due to excessive alcohol intake or lactic acid accumulation, can lead to a considerable increase in NADH levels, disrupting the balance of the NAD^+/NADH ratio.[4–8] In the human body, the biological functions of NOX are typically performed by other enzymes within a complex electron transport chain, which requires the coordinated action of multiple substrates and cannot catalyze NADH oxidation independently.[9] In contrast, NOX from fungi or plants possess a much simpler catalytic architecture, enabling more direct

NADH oxidation (Scheme 1).[10] However, these NOX can reduce O_2 to produce H_2O_2 for their physiological roles, which do not fulfill the requirements for efficient catalysis and byproduct-free reactions essential for human biological processes. To address this issue, researchers are eagerly exploring NOX mimics as potential alternatives.

Nanozymes as oxidase mimics have been well developed, which can activate O_2 and transfer electrons from substrates to O_2.[11–16] NOX-driven catalytic reactions contain two individual half-reactions: NADH dehydrogenation and O_2 reduction ($2e^-$ or $4e^-$ pathways).[17,18] The designed nanozyme should not only serve as an electron carrier, accepting electrons from NADH and transferring them to O_2, but also enable the catalysis of the more efficient $4e^-$ oxygen reduction pathway.[19] Due to tunable electronic structures and versatile active sites, noble metal nanomaterials exhibit superior enzyme-like activity and exceptional stability under harsh conditions.[20,21] However, research into noble metal nanomaterials as NADH oxidase mimics and their catalytic mechanisms remains largely unexplored.[22] This limitation stems from the considerable challenge of constructing electron transport structures (like Fe–S clusters or Cu ions) like natural NOX enzymes. As a result, their ability to activate both NADH and O_2 is constrained and the efficiency of proton and electron transfer between NADH and O_2 is significantly compromised.[10,22] More importantly, their limited electron transfer and utilization efficiency in redox reactions promote

[a]*State Key Laboratory of Green Pesticide, International Joint Research Center for Intelligent Biosensing Technology and Health, College of Chemistry, Central China Normal University, Wuhan, 430079, P.R. China. E-mail: czzhu@ccnu.edu.cn*

[b]*Institute of Nano-Science and Technology, College of Physical Science and Technology, Central China Normal University, Wuhan, 430079, P.R. China*

[c]*College of Material Chemistry and Chemical Engineering, Key Laboratory of Organosilicon Chemistry and Material Technology, Ministry of Education, Hangzhou Normal University, Hangzhou, 311121, P.R. China*
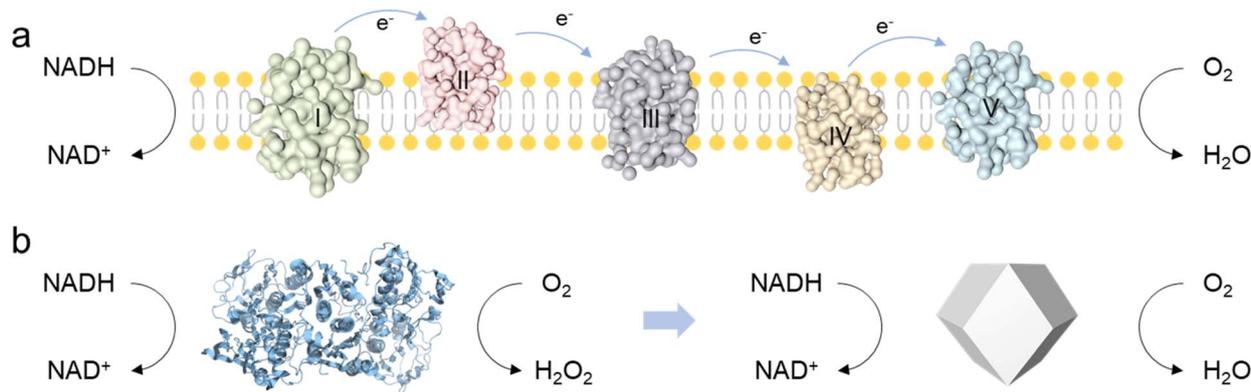
Scheme 1 (a) The NADH oxidative respiratory chain in the human body. (b) The catalytic pathway of NOX extracted from fungi or plants, and the proposed Ce_1Pt for NADH oxidation.

the generation of H_2O_2, which not only interferes with sensing accuracy but also limits their future safety in biological applications.

Herein, we synthesized atomic Ce-doped Ce_1Pt with abundant oxygen vacancy (OV) sites to boost the NOX-like activity for coenzyme regeneration. Experimental investigations demonstrated that the resultant Ce_1Pt possesses superior NOX-like activity to pristine Pt. Mechanism investigation indicates that the atomically dispersed Ce enhances the electron density of Pt and facilitates the formation of OV sites, thereby effectively promoting substrate adsorption. Unlike the $2e^-$ pathway seen in natural NOX, Ce_1Pt catalyzes the oxidation of NADH while facilitating the $4e^-$ reduction of oxygen, significantly enhancing the utilization of electrons extracted from NADH. Through synergistic integration with NAD^+-dependent natural enzyme systems, the as-engineered Ce_1Pt nanozyme demonstrated efficient cofactor recycling, enabling continuous bioconversion of metabolic substrates, including ethanol, acetaldehyde, and lactate. Then, a microfluidic platform was constructed for the monitoring of blood alcohol with a low limit of detection of 0.012 mM.

Results and discussion

Synthesis and morphology characterization of nanozymes

By using platinum(II) acetylacetonate ($Pt(acac)_2$) and cerium(III) acetylacetonate ($Ce(acac)_3$) as precursors, Ce_1Pt was successfully synthesized by a one-step hydrothermal method at 180 °C for 12 h (Fig. 1a).[23] As a control, Pt was synthesized using the same method, but only $Pt(acac)_2$ was used as the precursor. The morphology of the resultant Ce_1Pt, which possesses a uniform cuboctahedron morphology with an average size of ~20 nm, was characterized by transmission electron microscopy (TEM) (Fig. 1b). For comparison, Pt exhibits cubic morphology with a size similar to that of Ce_1Pt. The morphological changes imply that the introduction of Ce enhances the epitaxial growth of the crystal plane, leading to a transformation into the crystal phase structure of Pt (Fig. S1). As shown in Fig. 1c and S2b, high-resolution TEM (HRTEM) images reveal distinct lattice fringes of Ce_1Pt, with interplanar spacings of 0.24 nm, 0.20 nm, and 0.28 nm, corresponding to the (111), (100), and (110) planes of

Pt. In addition, energy-dispersive X-ray spectroscopy (EDS) analysis verifies the uniform distribution of Ce and Pt within the Ce_1Pt nanoparticles (Fig. 1d). The crystal structure of Ce_1Pt was thoroughly characterized using X-ray diffraction (XRD) (Fig. 1e). Five diffraction peaks observed at 39.8°, 46.2°, 67.5°, 81.3°, and 85.7° correspond to the (111), (100), (110), (311), and (222) planes of Pt (PDF#04-0802), indicating the consistent crystal structure of Pt. Further analysis using X-ray photoelectron spectroscopy (XPS) revealed that the high-resolution Pt 4f orbital can be divided into two paired peaks corresponding to Pt^0 and Pt^{2+}, indicating that platinum predominantly exists in its metallic state in both nanozymes (Fig. S3).[24] The Pt 4f orbital of Ce_1Pt exhibits a shift of 0.15 eV towards lower binding energy in comparison to the Pt nanozyme, which indicates that electrons are transferred from Ce atoms to Pt atoms and Pt atoms are enriched with electrons. As shown in Figure1f, three characteristic XPS peaks at approximately 530.6 eV, 531.3 eV, and 532.4 eV correspond to lattice oxygen, oxygen defects, and surface-adsorbed oxygen species, respectively.[25] The content of oxygen defects in Ce_1Pt is significantly higher than that in Pt, indicating that the introduction of Ce effectively removes certain oxygen elements, leading to the formation of more OVs within the Pt lattice.[26–28] Besides, electron paramagnetic resonance (EPR) displays a prominent Lorentzian line at a g value of around 2.003, suggesting a high density of unpaired electrons and defects in Ce_1Pt (Fig. S4).[29,30] As shown in Fig. 1g, the absence of significant Ce–Ce signals in the Fourier transform extended X-ray absorption fine structure (EXAFS) analysis further confirms the atomic dispersion of Ce atoms in Ce_1Pt (Fig. 1g).

NADH oxidase-like activity of nanozymes

Then, we systematically investigated the NOX-like activity of the resultant nanozymes. NADH, serving as a substrate for NOX, displays a characteristic UV absorption peak at 340 nm. Upon oxidation, the absorbance at this wavelength decreases, enabling the evaluation of the NOX-like activity of the nanozymes. As shown in Fig. 2a and b, Ce_1Pt can significantly lower the characteristic peak of NADH at 340 nm in comparison to Pt, indicating that the incorporation of Ce enhances the NOX-like
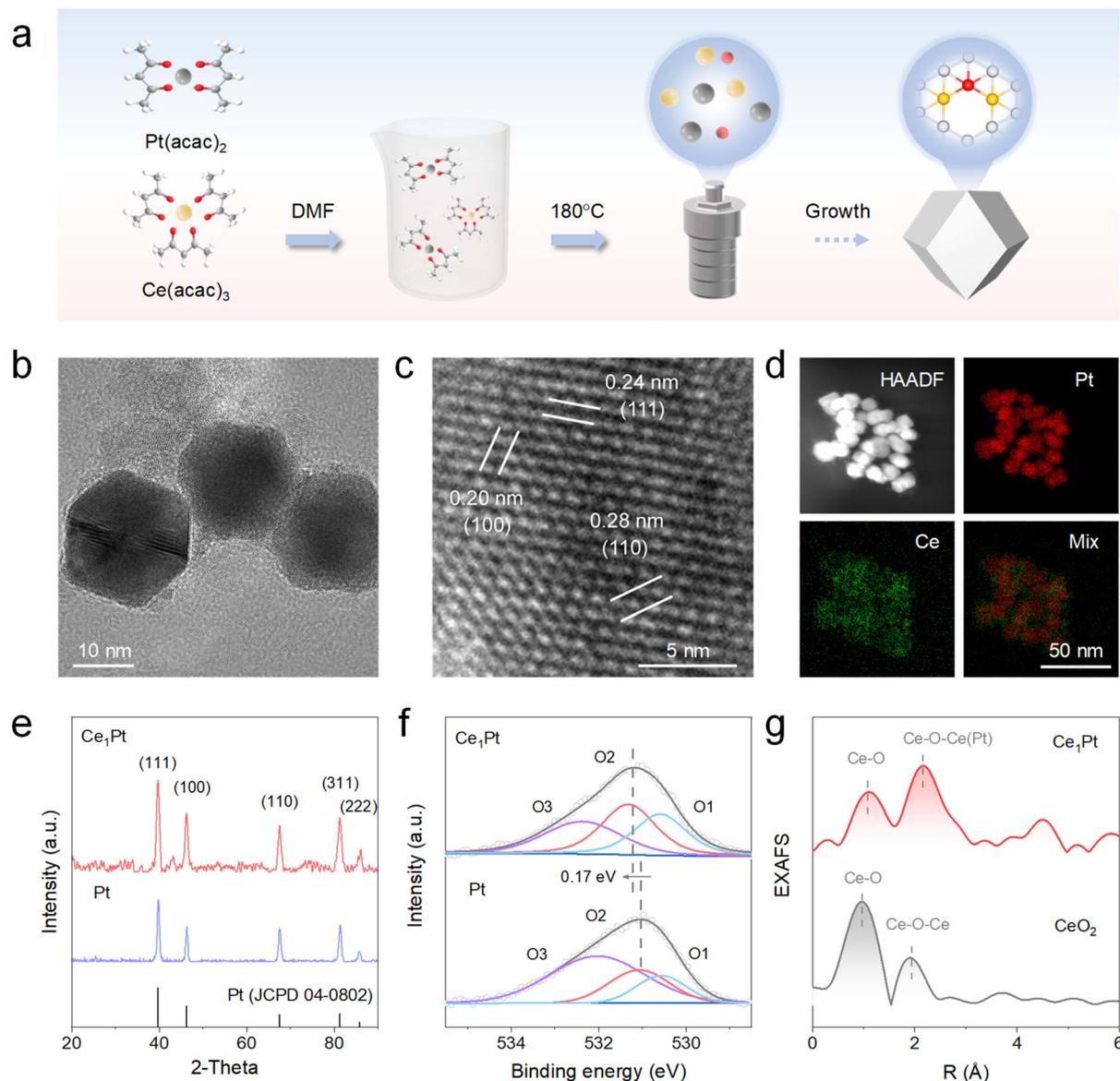
Fig. 1 (a) Schematic illustration for the synthesis of Ce₁Pt. (b) TEM image, (c) HRTEM image, (d) HAADF-STEM image, and the corresponding EDS mapping images of Ce₁Pt. (e) XRD patterns, (f) O 2p XPS spectra of nanozymes, and (g) EXAFS spectra of Ce₁Pt and CeO₂.

activity of nanozyme.[31–33] The NOX-like activity of Ce₁Pt exhibits a volcano-shaped dependence on pH, reaching maximum efficiency at pH 7.4, which aligns with physiological conditions (Fig. S5). Under the optimized pH conditions, kinetic experiments indicate that the nanozyme-involved catalytic reaction follows the Michaelis–Menten equation (Fig. 2c). The maximum reaction rate (V_{max}) of Ce₁Pt is 7.02×10^{-5} M min^{-1}, which is 1.24 times higher than that of Pt. Moreover, Ce₁Pt has a lower Michaelis constant (K_m), indicating a stronger affinity for the catalytic substrate in comparison to Pt (Table S1).[34,35] Notably, the kinetic parameters of Ce₁Pt surpass those reported for the majority of previously documented nanozymes. In O₂-saturated solutions, the oxidation rate of NADH is higher than that in N₂ and air-saturated solutions, confirming the essential role of O₂ in the simulated oxidase reaction (Fig. 2d). To evaluate the

advantages of Ce₁Pt, we compared it with several common nanozymes known for their NOX-like activity. The results demonstrated that it shows a significant advantage in NOX-like activity over other precious metals, metal oxides, and metal–organic frameworks (MOFs) (Fig. 2e). Moreover, Ce₁Pt benefits from the inherent stability of noble metals, allowing them to retain catalytic performance after being soaked or dried for 7 days. They are highly resistant to acidic and basic conditions and can be stored at room temperature for long periods without loss of activity (Fig. S6). Even after five cycles, Ce₁Pt and Pt retain their catalytic activity, highlighting their high stability (Fig. 2f).

Insights into the underlying catalytic mechanism

To verify the biological activity of regenerated coenzyme, we introduced glucose and glucose dehydrogenase (GDH) into the
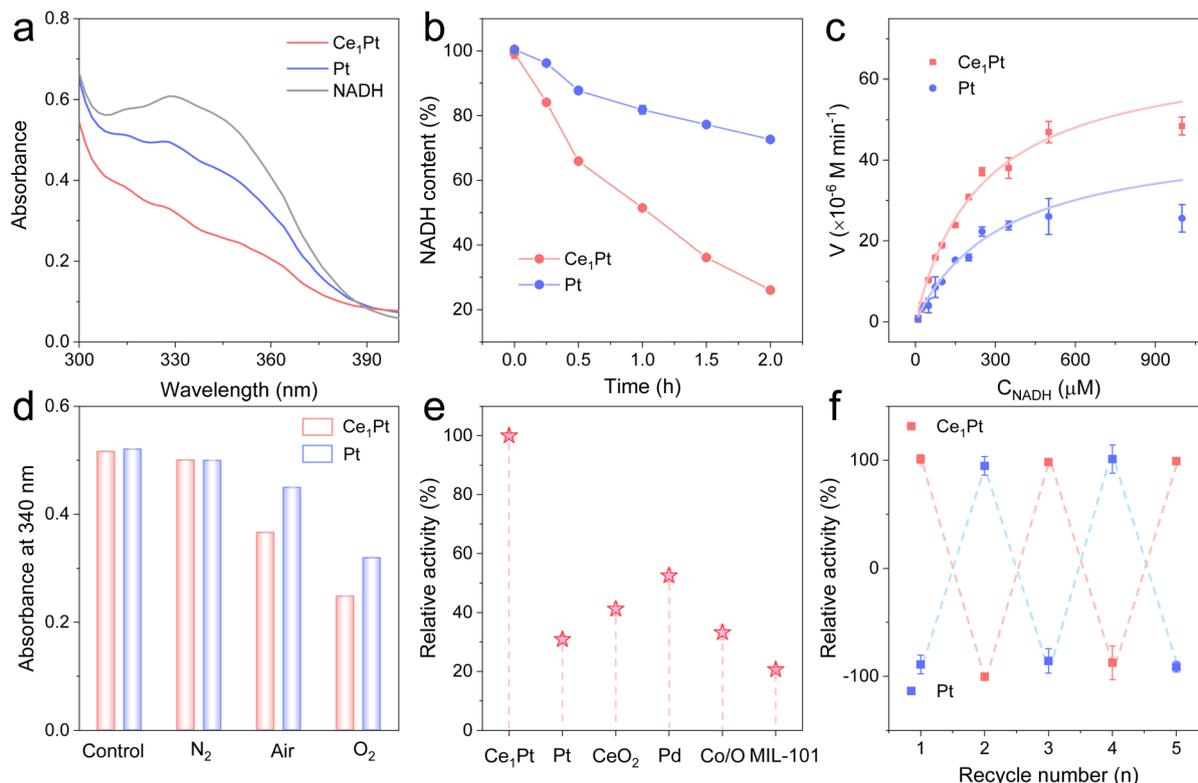
Fig. 2 (a) Absorption spectra and (b) time-dependent absorbance changes of the NADH oxidation reaction catalyzed by nanozymes. (c) The kinetic curve of nanozymes toward NADH. (d) UV-vis absorption at 340 nm of Ce_1Pt-catalyzed NADH oxidation in the N_2-, air-, and O_2-saturated solutions. (e) The relative NOX-like activity of different nanozymes. (f) The cycling stability of nanozymes.

reaction system (Fig. 3a and S7). It is observed that after a 30-minute reaction between NADH and the nanozymes, the absorbance at 340 nm decreases, indicating that both Ce_1Pt and Pt can effectively oxidize NADH to NAD^+ during the process. Then, after the removal of the nanozymes, the addition of glucose and GDH leads to a renewed increase in absorbance. As shown in Fig. 3b, mass spectrometry analysis shows the changes in molecular mass in the solution before and after the reaction. Before the reaction, the mass spectrum displayed only a peak at 709.4, corresponding to the molecular mass of NADH. After the reaction, the peak at 709.4 significantly weakened, and a new peak appeared at 708.4, corresponding to the molecular mass of NAD^+, which indicates that Ce_1Pt can oxidize NADH to NAD^+. Using 5-(2-Carboxyphenyl)-5-methyl-1-pyrroline-N-oxide (CYPMPO) as a spin-trapping agent, EPR was employed to detect the free radicals generated during the Ce_1Pt-catalyzed oxidation of NADH. As shown in Fig. 3c, a strong signal of the CYPMPO-NAD adduct was detected by EPR after 10 minutes of reaction catalyzed by Ce_1Pt, confirming the formation of the $NAD^{\cdot}$ intermediate. Then, electrochemical measurement was used to examine the selectivity of O_2 reduction on nanozymes. As depicted in Fig. 3d, nanozymes were deposited onto the disk electrode of a rotating ring-disk setup.[36]

During the negative scan, the nanozyme acts as a catalyst, promoting the transfer of electrons from the electrode to O_2 and catalyzing the ORR. The results indicate that both the disk current and ring current increase concurrently, suggesting the

reduction of O_2. The H_2O_2 yield (% H_2O_2) for Ce_1Pt was measured at 0.58% with an electron transfer number of 3.99, confirming their $4e^-$ pathways in the O_2-saturated PBS buffer (Fig. S8a). HRP colorimetric assay also shows no color development of TMB, which confirms that the material prefers the four-electron pathway (Fig. S8b). Then, in situ attenuated total reflection FTIR (ATR-FTIR) spectroscopy and Raman spectroscopy were employed to monitor the NADH oxidation process in real time. As shown in Fig. 3e, the intensity of the C–N signals ($\sim$1058 cm^{-1}) and C–H signals ($\sim$1395 cm^{-1}) decreases significantly, while the C=N signals ($\sim$1602 cm^{-1}) progressively increase over time, indicating the oxidation of NADH. Furthermore, the gradually increasing peak intensities at $\sim$3200 cm^{-1} indicate the progressive formation of H_2O. The emergence and increased intensity of the Raman band at $\sim$590 cm^{-1} during NADH oxidation are attributed to defect-induced lattice vibrational distortion in Ce-based oxides, which is associated with OVs. This observation confirms that OVs are dynamically engaged in the catalytic process (Fig. 3f).[37]

DFT calculations of the catalytic process

To gain deeper insight into the catalytic behavior of nanozymes, the mechanism was explored using density functional theory (DFT) calculations (Fig. S9). The adsorption energy of O_2 on the OVs of Ce_1Pt was calculated to be -1.80 eV, significantly lower than that of Pt (-0.49 eV), highlighting the superior adsorption
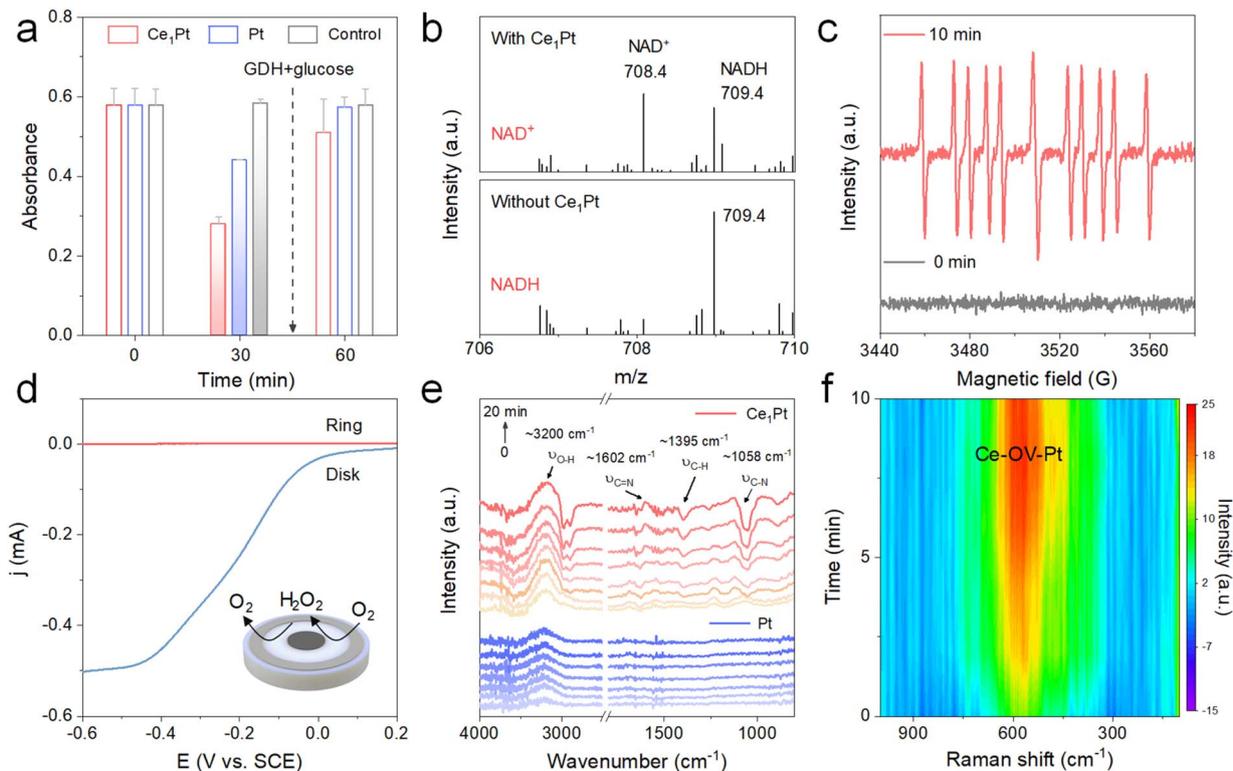
Fig. 3 (a) Time-dependent absorption change at 340 nm. (b) Mass spectra of the NADH oxidation reaction. (c) EPR spectra of the spin adducts formed from CYPMPO in the reaction of NADH and Ce$_1$Pt. (d) RRDE measurement of the selective oxygen reduction of Ce$_1$Pt in the O$_2$-saturated electrolyte. (e) In situ ATR-FTIR spectra and (f) In situ Raman spectra of the nanozyme-catalyzed NADH oxidation reaction.

capability of Ce$_1$Pt (Fig. 4a). To investigate electron transfer between O$_2$ and the nanozymes, charge density difference calculations were conducted (Fig. 4b and c, and S10). Upon O$_2$ adsorption at the OVs, significant electron transfer was observed within the Pt and Ce sites, resulting in a decrease in electron density around the Pt or Ce atoms and an increase in electron density around the O$_2$. As illustrated in Fig. 4d, the energy changes associated with the *OOH to *O step are calculated to be −2.68 eV for Ce$_1$Pt and −2.49 eV for Pt. These values are notably lower than those of the *OOH to H$_2$O$_2$ step (0.66 eV for Ce$_1$Pt and −0.42 eV for Pt), highlighting that the Ce$_1$Pt nanozymes exhibit a strong preference for the 4e⁻ pathway during O$_2$ reduction. In addition, as shown in Fig. 4e, the d-band centers of both Ce$_1$Pt and Pt are −2.31. While the d-band center of Ce$_1$Pt remains unchanged, the introduction of Ce lowers the p-band center of the adsorbed O, resulting in greater overlap with the d-band center. This suggests that the incorporation of Ce enhances the interaction with oxygen intermediates, thereby promoting the oxygen reduction reaction. These findings indicate that Ce$_1$Pt facilitates the dehydrogenation of NADH into a NAD˙ intermediate, followed by the transfer of electrons from NADH to O$_2$, which is subsequently reduced to H$_2$O (Fig. 4f).

Practical sensing applications

NAD⁺-dependent dehydrogenases in the human body, including alcohol dehydrogenase (ADH), aldehyde

dehydrogenase (ALDH), and lactate dehydrogenase (LDH), drive substrate oxidation for metabolic homeostasis. However, NADH accumulation under substrate overload induces reverse catalysis, creating a vicious cycle of redox imbalance and pathological substrate retention (Fig. 5a and b).[38–41] Especially for LDH, since most commercially available LDHs have higher reverse reaction activity, it becomes challenging to facilitate the forward reaction effectively.[20] Therefore, we aim to leverage nanozymes for in situ coenzyme regeneration, which helps suppress the reverse reaction and restore metabolic balance. As shown in Fig. 5c, the characteristic peak of NADH at 340 nm is restored after the addition of ethanol and ADH. This demonstrates that the nanozyme can oxidize NADH to NAD⁺, as a coenzyme for ADH in the ethanol metabolism process. Similarly, the absorbance of NADH at 340 nm is also recovered upon the addition of acetaldehyde and ADH, or lactate and LDH (Fig. 5d and e). It is noteworthy that NAD⁺ alone cannot facilitate lactate dehydrogenation catalyzed by LDH, and the reaction occurs exclusively in the presence of both NADH and Ce$_1$Pt. This is because the reverse reaction rate catalyzed by LDH in the human body is significantly higher than its forward reaction rate, which can only be driven under conditions where Ce$_1$Pt continuously catalyzes the regeneration of NAD⁺. Proton nuclear magnetic resonance spectroscopy (¹H NMR) confirmed that after the addition of Ce$_1$Pt, ADH can effectively metabolize ethanol. When ethanol is used as the substrate, with ADH, ALDH, and the nanozyme added simultaneously, the metabolic product of
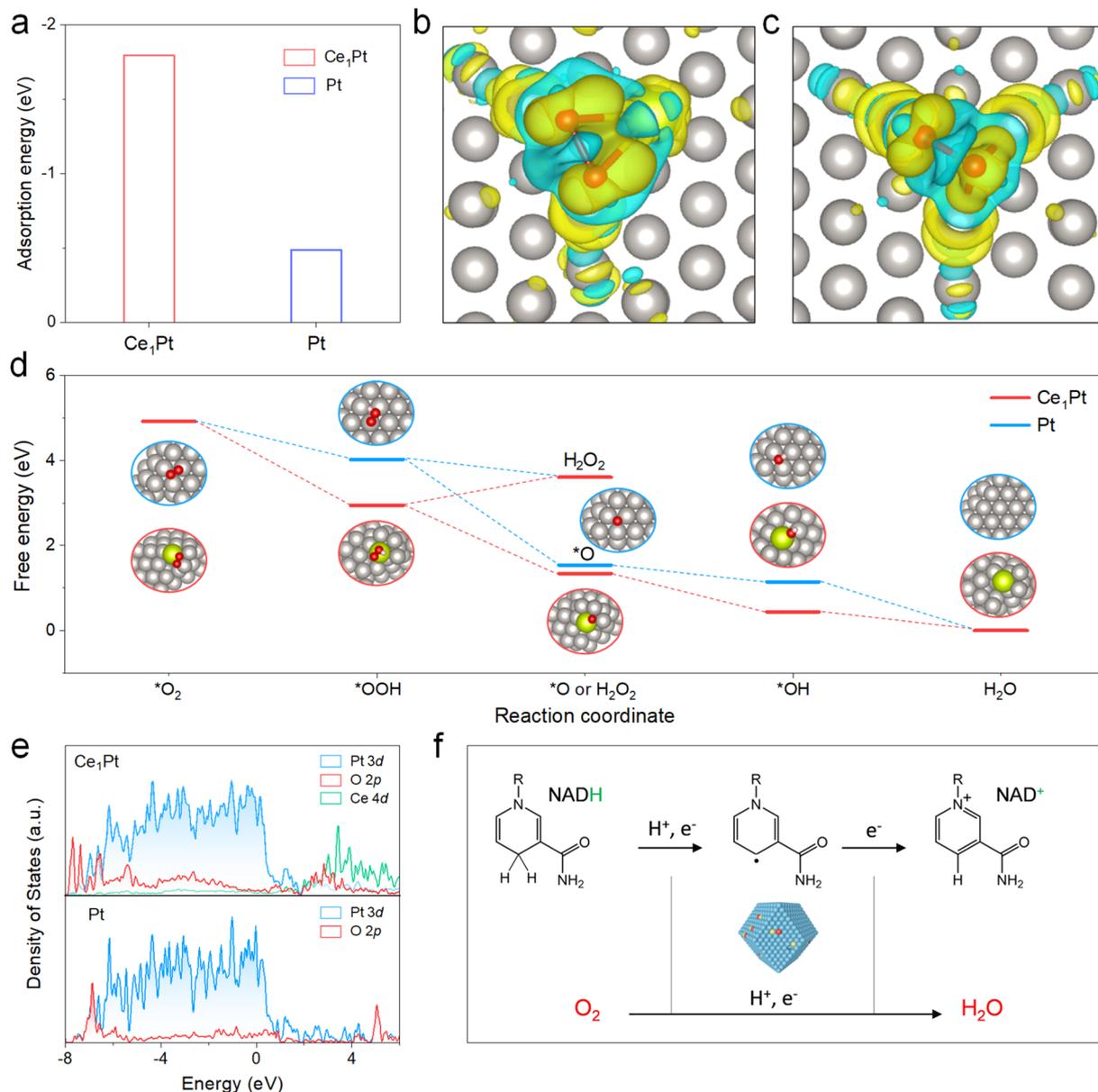
© 2026 The Author(s). Published by the Royal Society of Chemistry

Fig. 4 (a) The absorption energy of nanozymes to O_2. Calculated charge density differences to study the bonding interactions and the charge transfer of (b) Ce_1Pt and (c) Pt among Pt, Ce, and O atoms. The yellow/blue isosurfaces denote an increase/decrease in electron density, and the grey, red, and yellow spheres represent Pt, O, and Ce atoms, respectively. (d) The free energy diagram of nanozymes determined by the DFT studies. (e) Projected DOS of Pt-d, Ce-d, and O-p orbitals of nanozymes. (f) Proposed NOX-like mechanism of Ce_1Pt involving NADH oxidation and O_2 reduction.

the reaction is acetic acid (Fig. S11).[42,43] Similarly, Ce_1Pt also facilitates ALDH in metabolizing acetaldehyde and promotes LDH in converting lactate to pyruvate (Fig. S12).[44,45] This demonstrates that the proposed NOX mimics exhibit the function of *in situ* coenzyme regeneration for inhibiting reverse reactions and promoting substrate metabolism. Furthermore, real-time assessment of *in vivo* metabolite concentrations offers a practical method for monitoring systemic health.[46,47] This clinical relevance has accelerated the development of microfluidic platforms featuring integrated flow reactors, miniaturized architecture, and automated operation capability (Fig. 5f). The samples (ethanol), NAD^+, ADH, and PBS buffer (pH 7.4)

were introduced into the first reaction chamber for NADH production. Then, NaAc-HAc buffer (pH 3.0) was introduced to push the solution into the second reaction chamber and adjust the pH to around 3.5. The intrinsic oxidase-like activity of Ce_1Pt induces competitive adsorption between TMB and NADH as substrates. As the blood alcohol concentration increases, the absorbance of the TMB-derived chromogenic product decreases. Based on this mechanism, we engineered a highly sensitive ratiometric sensor for quantifying NADH in blood ranging from 0.02–43 mM, with a low limit of detection of 0.012 mM mg 100 mL^{-1} (Fig. 5g).
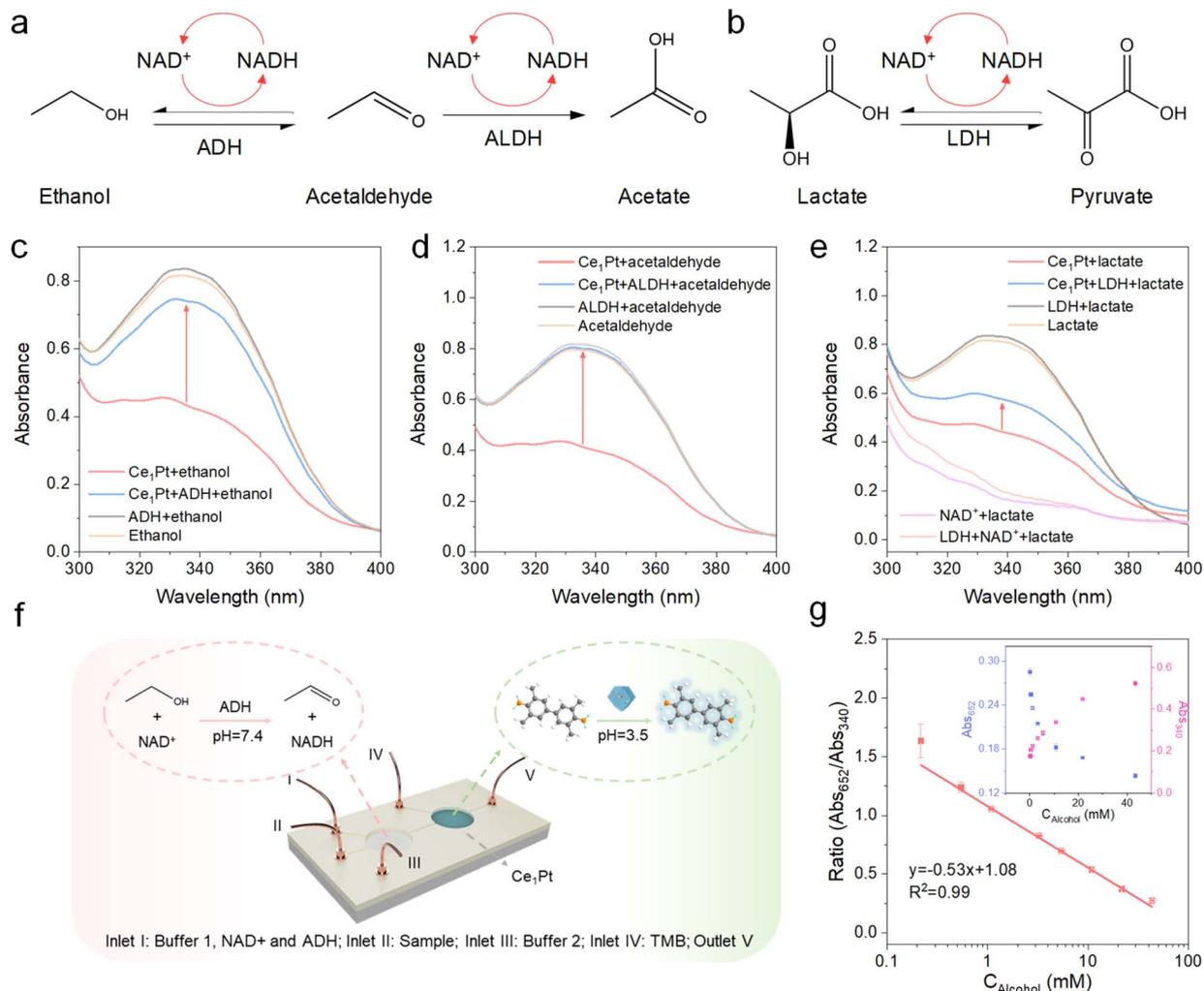
Fig. 5 (a and b) Schematic illustration of the ethanol, aldehyde, and lactate metabolic processes. Absorption spectra of NADH oxidation and regeneration reaction catalyzed by nanozymes with (c) ADH, (d) ALDH, or (e) LDH. (f) Nanozyme reaction system in a microfluidic device. (g) The ratiometric calibration curves for the detection of alcohol in blood. Inset: colorimetric response to different concentrations of alcohol in blood.

Conclusions

In summary, inspired by natural enzymes, we developed Ce_1Pt nanozymes with NOX-like activity through the doping of atomic Ce. The introduction of Ce effectively reconstructed the Pt lattice and promoted the formation of OVs within the materials, and the NOX-like activity of the resultant Ce_1Pt increased by 1.5 times that of Pt. Mechanistic studies reveal that Ce–OV sites enhance O_2 adsorption, effectively reducing the reaction energy change and accelerating the reaction process. Moreover, the incorporation of Ce promotes the preference for the $4e^-$ O_2 reduction pathway in Ce_1Pt, thereby reducing H_2O_2 generation and facilitating NADH oxidation. By harnessing its NOX-like activity, Ce_1Pt can effectively facilitate *in situ* coenzyme regeneration, promoting the forward reaction of the enzyme-catalyzed reaction and thereby accelerating substrate metabolism. Finally, Ce_1Pt was successfully utilized in fabricating a microfluidic chip for detecting alcohol in blood.

Ethical statement

All experiments were performed in accordance with the guidelines of the "Declaration of Helsinki" and approved by the ethics committee at "China Resources & Wisco General Hospital, Wuhan University of Science and Technology (Wuhan, P.R. China)". Informed consents were obtained from human participants of this study. All human samples were de-identified of all identifying information. Informed and permitted consent was obtained from each subject in all clinical experiments of this manuscript.

Author contributions

Conceptualization, Y. T. and C. Z.; methodology, Y. T., Y. C., and P. Q.; investigation, Y. T., Y. C., R. L., W. J., and W. G.; writing – original draft, Y. T. and C. Z.; writing – review & editing, Y. T. and C. Z.; funding acquisition, W. G. and C. Z.; resources, H. S., W. G. and C. Z.; supervision, C. Z.

Conflicts of interest

There are no conflicts to declare.

Data availability

The data supporting this article have been included as part of the supplementary information (SI). Supplementary information: SI methods, Fig. S1–S12 and Table S1. See DOI: https://doi.org/10.1039/d6sc00612d.

Acknowledgements

Notes and references

1 L. Guarente, *Science*, 2016, **352**, 1396–1397.

2 M. E. Migaud, M. Ziegler and J. A. Baur, *Nat. Rev. Mol. Cell Biol.*, 2024, **25**, 822–840.

3 D. V. Titov, V. Cracan, R. P. Goodman, J. Peng, Z. Grabarek and V. K. Mootha, *Science*, 2016, **352**, 231–235.

4 R. P. Goodman, A. L. Markhard, H. Shah, R. Sharma, O. S. Skinner, C. B. Clish, A. Deik, A. Patgiri, Y.-H. H. Hsu, R. Masia, H. L. Noh, S. Suk, O. Goldberger, J. N. Hirschhorn, G. Yellen, J. K. Kim and V. K. Mootha, *Nature*, 2020, **583**, 122–126.

5 X. Wang and H. H. P. Yiu, *ACS Catal.*, 2016, **6**, 1880–1886.

6 A. Patgiri, O. S. Skinner, Y. Miyazaki, G. Schleifer, E. Marutani, H. Shah, R. Sharma, R. P. Goodman, T.-L. To, X. Robert Bao, F. Ichinose, W. M. Zapol and V. K. Mootha, *Nat. Biotechnol.*, 2020, **38**, 309–313.

7 W. J. Quinn, J. Jiao, T. TeSlaa, J. Stadanlick, Z. Wang, L. Wang, T. Akimova, A. Angelin, P. M. Schäfer, M. D. Cully, C. Perry, P. K. Kopinski, L. Guo, I. A. Blair, L. R. Ghanem, M. S. Leibowitz, W. W. Hancock, E. K. Moon, M. H. Levine, E. B. Eruslanov, D. C. Wallace, J. A. Baur and U. H. Beier, *Cell Rep.*, 2020, **33**, 108500.

8 Y. Liu, J. Du, M. Yan, M. Y. Lau, J. Hu, H. Han, O. O. Yang, S. Liang, W. Wei, H. Wang, J. Li, X. Zhu, L. Shi, W. Chen, C. Ji and Y. Lu, *Nat. Nanotechnol.*, 2013, **8**, 187–192.

9 D. Zhu, M. Zhang, C. Wang, P. Gai and F. Li, *Chem. Mater.*, 2022, **34**, 11072–11080.

10 J. Chen, X. Zheng, J. Zhang, Q. Ma, Z. Zhao, L. Huang, W. Wu, Y. Wang, J. Wang and S. Dong, *Natl. Sci. Rev.*, 2022, **9**, nwab186.

11 Y. Huang, J. Ren and X. Qu, *Chem. Rev.*, 2019, **119**, 4357–4412.

12 C. Peng, R. Pang, J. Li and E. Wang, *Adv. Mater.*, 2024, **36**, 2211724.

13 J. Wu, X. Wang, Q. Wang, Z. Lou, S. Li, Y. Zhu, L. Qin and H. Wei, *Chem. Soc. Rev.*, 2019, **48**, 1004–1076.

14 J. Chen, X. Liu, G. Zheng, W. Feng, P. Wang, J. Gao, J. Liu, M. Wang and Q. Wang, *Small*, 2023, **19**, 2205924.

15 J. Chen, Q. Ma, M. Li, D. Chao, L. Huang, W. Wu, Y. Fang and S. Dong, *Nat. Commun.*, 2021, **12**, 3375.

16 Q. Liu, A. Zhang, R. Wang, Q. Zhang and D. Cui, *Nano-Micro Lett.*, 2021, **13**, 154.

17 A. Rodriguez-Abetxuko, A. Reifs, D. Sánchez-deAlcázar and A. Beloqui, *Angew. Chem., Int. Ed.*, 2022, **61**, e202206926.

18 X. Liu, Z. Wan, K. Chen, Y. Yan, X. Li, Y. Wang, M. Wang, R. Zhao, J. Pei, L. Zhang, S. Sun, J. Li, X. Chen, Q. Xin, S. Zhang, S. Liu, H. Wang, C. Liu, X. Mu and X.-D. Zhang, *Nano Lett.*, 2024, **24**, 4924–4935.

19 J. Liu, B. Yu, M. Rong, W. Sun and L. Lu, *Nano Today*, 2024, **54**, 102113.

20 D. Jiang, D. Ni, Z. T. Rosenkrans, P. Huang, X. Yan and W. Cai, *Chem. Soc. Rev.*, 2019, **48**, 3683–3704.

21 L. Gao, H. Wei, S. Dong and X. Yan, *Adv. Mater.*, 2024, **36**, 2305249.

22 D. Li, J. He, G. Ding, Y. Xin, F. Feng, S. Ma, L. Lin, E. Wang and J. Wang, *Adv. Healthcare Mater.*, 2025, **14**, 2402785.

23 H. Rong, J. Mao, P. Xin, D. He, Y. Chen, D. Wang, Z. Niu, Y. Wu and Y. Li, *Adv. Mater.*, 2016, **28**, 2540–2546.

24 R. Feng, D. Li, H. Yang, C. Li, Y. Zhao, G. I. N. Waterhouse, L. Shang and T. Zhang, *Adv. Mater.*, 2024, **36**, 2309251.

25 C. T. Campbell and C. H. F. Peden, *Science*, 2005, **309**, 713–714.

26 G. Hou, Q. Wang, D. Xu, H. Fan, K. Liu, Y. Li, X.-K. Gu and M. Ding, *Angew. Chem., Int. Ed.*, 2024, **63**, e202402053.

27 X. Luo, H. Zhao, X. Tan, S. Lin, K. Yu, X. Mu, Z. Tao, P. Ji and S. Mu, *Nat. Commun.*, 2024, **15**, 8293.

28 F. Xu, Y. He, J. Zhang, G. Liang, C. Liu and J. Yu, *Angew. Chem., Int. Ed.*, 2025, **64**, e202414672.

29 W. Xu, H. Zhong, Y. Wu, Y. Qin, L. Jiao, M. Sha, R. Su, Y. Tang, L. Zheng, L. Hu, S. Zhang, S. P. Beckman, W. Gu, Y. Yang, S. Guo and C. Zhu, *Proc. Natl. Acad. Sci. U. S. A.*, 2023, **120**, e2220315120.

30 Y. Wu, W. Xu, L. Jiao, Y. Tang, Y. Chen, W. Gu and C. Zhu, *Mater. Today*, 2022, **52**, 327–347.

31 Y. Tang, Y. Chen, Y. Wu, W. Xu, Z. Luo, H.-R. Ye, W. Gu, W. Song, S. Guo and C. Zhu, *Nano Lett.*, 2023, **23**, 267–275.

32 S.-M. Jo, F. R. Wurm and K. Landfester, *Angew. Chem., Int. Ed.*, 2021, **60**, 7728–7734.

33 K.-X. Teng, L.-Y. Niu, N. Xie and Q.-Z. Yang, *Nat. Commun.*, 2022, **13**, 6179.

34 Y. Tang, Y. Wu, W. Xu, L. Jiao, Y. Chen, M. Sha, H.-R. Ye, W. Gu and C. Zhu, *Anal. Chem.*, 2022, **94**, 1022–1028.

35 W. Jiang, Y. Wu, R. Su, W. Xu, W. Yang, Y. Qiu, Y. Cai, C. Wang, L. Hu, W. Gu and C. Zhu, *Nano Lett.*, 2024, **24**, 9635–9642.

36 Y. Tang, X. Liu, P. Qi, W. Xu, Y. Wu, Y. Cai, W. Gu, H. Sun, C. Wang and C. Zhu, *Nano Lett.*, 2024, **24**, 9974–9982.

37 Y. Huang, B. Long, M. Tang, Z. Rui, M.-S. Balogun, Y. Tong and H. Ji, *Appl. Catal., B*, 2016, **181**, 779–787.

38 K. G. Hicks, A. A. Cluntun, H. L. Schubert, S. R. Hackett, J. A. Berg, P. G. Leonard, M. A. Ajalla Aleixo, Y. Zhou, A. J. Bott, S. R. Salvatore, F. Chang, A. Blevins, P. Barta, S. Tilley, A. Leifer, A. Guzman, A. Arok, S. Fogarty, J. M. Winter, H.-C. Ahn, K. N. Allen, S. Block, I. A. Cardoso, J. Ding, I. Dreveny, W. C. Gasper, Q. Ho, A. Matsuura, M. J. Palladino, S. Prajapati, P. Sun, K. Tittmann, D. R. Tolan, J. Unterlass, A. P. VanDemark, M. G. Vander Heiden, B. A. Webb, C.-H. Yun, P. Zhao, B. Wang, F. J. Schopfer, C. P. Hill, M. C. Nonato, F. L. Muller, J. E. Cox and J. Rutter, *Science*, 2023, **379**, 996–1003.

39 H. Chen, Y. Li, H. Li, X. Chen, H. Fu, D. Mao, W. Chen, L. Lan, C. Wang, K. Hu, J. Li, C. Zhu, I. Evans, E. Cheung, D. Lu, Y. He, A. Behrens, D. Yin and C. Zhang, *Nature*, 2024, **631**, 663–669.

40 J. Zhang, Y. Guo, X. Zhao, J. Pang, C. Pan, J. Wang, S. Wei, X. Yu, C. Zhang, Y. Chen, H. Yin and F. Xu, *Nat. Rev. Cardiol.*, 2023, **20**, 495–509.

41 A. Ghaddar, V. K. Mony, S. Mishra, S. Berhanu, J. C. Johnson, E. Enriquez-Hesles, E. Harrison, A. Patel, M. K. Horak, J. S. Smith and E. J. O'Rourke, *Curr. Biol.*, 2023, **33**, 1036–1046.

42 F. Gao, G. Liu, A. Chen, Y. Hu, H. Wang, J. Pan, J. Feng, H. Zhang, Y. Wang, Y. Min, C. Gao and Y. Xiong, *Nat. Commun.*, 2023, **14**, 6783.

43 H. Wang, H. Zheng, L. Ling, Q. Fang, L. Jiao, L. Zheng, Y. Qin, Z. Luo, W. Gu, W. Song and C. Zhu, *ACS Nano*, 2022, **16**, 21266–21274.

44 E. T. Montrazi, K. Sasson, L. Agemy, A. Scherz and L. Frydman, *Sci. Adv.*, 2024, **10**, eadm8600.

45 Q. Wu, X. Liang, K. Wang, J. Lin, X. Wang, P. Wang, Y. Zhang, Q. Nie, H. Liu, Z. Zhang, J. Liu, Y. Pang and C. Jiang, *Cell Metab.*, 2021, **33**, 1988–2003e1987.

46 X. Wang, Y. Luo, K. Huang and N. Cheng, *Adv. Agrochem.*, 2022, **1**, 3–6.

47 Y. Tang, Y. Wu, W. Xu, L. Jiao, W. Gu, C. Zhu, D. Du and Y. Lin, *Adv. Agrochem.*, 2022, **1**, 12–21.